The unique radar properties of silicic lava domes

Jeffrey J. Plaut,[1] Steven W. Anderson,[2] David A. Crown,[3] Ellen R. Stofan,[4] and Jakob J. van Zyl[1]

[1] Silicic lava domes exhibit distinct morphologic characteristics at scales of centimeters to kilometers. Multiparameter radar observations capture the unique geometric signatures of silicic domes in a set of radar scattering properties that are unlike any other natural geologic surfaces. Backscatter cross-section values are among the highest observed on terrestrial lava flows and show only a weak decrease with incidence angle. Cross-polarization backscatter (HV) shows a unique behavior, increasing with increasing wavelength. Circular polarization ratios are relatively high, in the 0.3–0.95 range, and increase with increasing wavelength. Field measurements of boulder size frequency distributions and microtopography indicate that silicic dome surfaces are among the roughest ever measured. Rms heights at a 1 m lateral scale range from 13 cm to 50 cm. Rms slopes at 1 m spacing range from 12 to 43 degrees. Modeling of the scattering behavior suggests it results from a combination of rough surface (facet) scattering and scattering from block edges that act as a random collection of dipoles. The unusual wavelength dependence of the radar parameters appears to result from a higher component of edge scattering at large wavelengths, producing, for example, higher cross-polarized backscatter at P band (68 cm). Steep-sided volcanic domes on Venus superficially resemble terrestrial silicic domes in plan view gross morphology, but few similarities remain when the radar scattering and three-dimensional shapes of the features are compared. The unique radar scattering properties suggest that such volcanic surfaces can be identified with multiparameter radar observations in future planetary radar missions and in active terrestrial volcanoes, where dome development can represent serious hazards. *INDEX TERMS:* 5464 Planetology: Solid Surface Planets: Remote sensing; 5480 Planetology: Solid Surface Planets: Volcanism (8450); 6295 Planetology: Solar System Objects: Venus; 6207 Planetology: Solar System Objects: Comparative planetology; 8429 Volcanology: Lava rheology and morphology; *KEYWORDS:* radar, remote sensing, volcanology

1. Introduction

[2] Investigation of volcanic landforms and surfaces with remote sensing has become an important element in geologic studies of the surfaces of the planets. Interpretation of data from planetary missions requires an understanding of related phenomena on Earth, a task that often includes a search for appropriate terrestrial analogues to planetary features. The Magellan radar mapping mission to Venus revealed a variety of volcanic features, and the interpretation of the radar images inspired a number of studies utilizing radar remote sensing of terrestrial volcanoes and lava flows [e.g., *Greeley and Martel*, 1988; *Ford et al.*, 1989; *Gaddis et al.*, 1989, 1990; *Campbell and Campbell*, 1992; *Arvidson et al.*, 1993; *Mouginis-Mark*, 1995; *Campbell and Shepard*, 1996]. A remarkable finding from Magellan was a class of apparently volcanic landforms referred to as "steep-sided" or "pancake" domes [*Head et al.*, 1992; *Pavri et al.*, 1992; *McKenzie et al.*, 1992; *Fink et al.*, 1993; *Bridges*, 1997; *Stofan et al.*, 2000]. The gross morphology of these features was reminiscent of silicic lava domes on Earth, and early workers suggested that they represented viscous lava flows, silicic in composition [*McKenzie et al.*, 1992] or alternatively, less silicic lavas with enhanced gas bubble content [*Pavri et al.*, 1992].

[3] In this paper, we examine the radar scattering behavior of the silicic domes of the Inyo volcanic chain, California, with an emphasis on the scattering characteristics that distinguish the dome surfaces from other lava flow surfaces. We then incorporate field measurements of the roughness characteristics of the dome surfaces into an analysis of the mechanisms of radar scattering that produce the unique signatures. Finally, we compare the observations

---

[1]Jet Propulsion Laboratory, California Institute of Technology, Pasadena, California, USA.
[2]Department of Science, Black Hills State University, Spearfish, South Dakota, USA.
[3]Planetary Science Institute, Tucson, Arizona, USA.
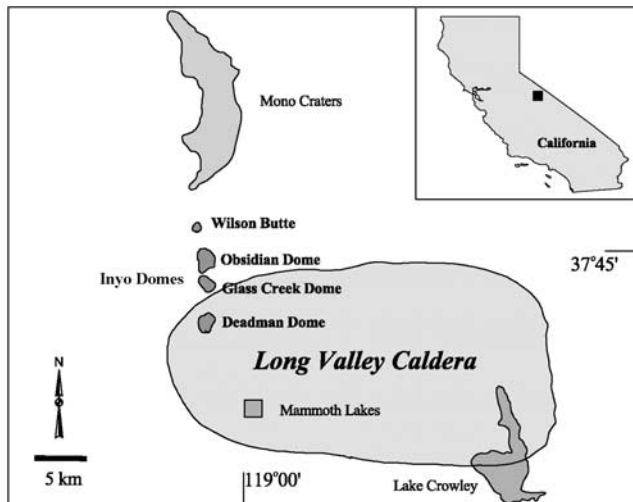[4]Proxemy Research, Rectortown, Virginia, USA.

Figure 1. Map of study area. Inyo domes occur along a north-south trend crossing the northwest boundary of the Long Valley caldera.

of terrestrial silicic domes with those of steep-sided domes on Venus, and discuss the implications for the formation of the Venusian domes.

2. Geologic Description

[4] The Inyo chain is a series of silicic lava flows and explosion pits that cut across the northern margin of Long Valley caldera in eastern California (Figure 1). The most prominent features in this chain are four recently emplaced rhyolitic extrusions. Deadman Dome, Glass Creek Dome, and Obsidian Dome formed after a series of explosive eruptions 550–650 years ago, and Wilson Butte extruded approximately 1200–1350 years ago [*Miller*, 1985]. A series of small pyroclastic eruptions preceded the emplacement of the three youngest domes in the Inyo chain [*Miller*, 1985]. An en echelon dike system [*Fink*, 1985; *Reches and Fink*, 1988] that apparently tapped more than one magma body fed the dome-building eruptions [*Eichelberger et al.*, 1988]. The domes vary in volume, ranging from 0.026 km³ for Wilson Butte (roughly cylindrical in shape with an average radius of 320 m and an average thickness of 80 m), to 0.17 km³ for Obsidian Dome [*Miller*, 1985] (see section 3.3 below for new estimates of volumes). *Anderson and Fink* [1992] estimated an effusion rate of 106 m³/s for the Glass Creek Dome from studies of crease structure formation. This rate is somewhat higher than those measured for lobes at the Mount St. Helens dome (1.4–40.3 m³/s [*Anderson and Fink*, 1990]).

[5] Two distinct lava types comprise the three most recently emplaced Inyo domes: a finely porphyritic (phenocrysts generally <2 mm) and a coarsely porphyritic rhyolite (phenocrysts generally 3–10 mm) [*Bailey et al.*, 1976, 1983; *Sampson*, 1987; *Sampson and Cameron*, 1987; *Swanson et al.*, 1989]. The finely porphyritic rhyolite shows both chemical and mineralogical zonation [*Bailey et al.*, 1976], suggesting that mingling of two different magma types occurred during emplacement [*Vogel et al.*, 1989]. According to detailed surface mapping by *Sampson* [1987], Deadman Dome consists primarily of coarsely porphyritic lava, Glass Creek Dome contains roughly equal amounts of coarsely and finely porphyritic varieties, and Obsidian Dome is entirely finely porphyritic rhyolite. Wilson Butte consists of a phenocryst-poor rhyolite that is megascopically similar to the finely porphyritic rhyolite found at the other Inyo domes.

[6] Surface and drilling studies reveal a complex stratigraphy of glassy and vesicular textures within the finely porphyritic lavas of the Inyo chain. Rhyolitic extrusions typically consist of a surface layer of finely vesicular pumice (FVP) underlain by a zone of obsidian [*Fink*, 1983; *Fink and Manley*, 1987; *Manley and Fink*, 1988]. Beneath this upper obsidian zone, a layer of coarsely vesicular pumice (CVP) forms where volatiles released in the flow interior accumulate beneath the cooled crust of obsidian and FVP. This layer has a lower density than the overlying material and may rise to the surface as regularly spaced diapirs [*Fink and Manley*, 1987; *Manley and Fink*, 1988]. These diapirs may then deform as the flow surface compresses during ridge formation [*Fink*, 1983]. Small crease structures commonly cut across CVP diapirs due to extensional stresses accumulating perpendicular to the direction of compression during ridge formation [*Anderson and Fink*, 1992].

3. Radar Data Analysis

[7] Multiple-wavelength polarimetric SAR (synthetic aperture radar) data were acquired over the Inyo domes by the NASA/JPL AIRSAR system in August, 1993 (Figure 2a). Data were acquired at three incidence angles, using the P (68 cm), L (24 cm) and C band (5.6 cm) quad-polarization modes [*van Zyl et al.*, 1987]. The quad-polarization mode captures the full scattering matrix for each ~10 m pixel, allowing synthesis of any combination of transmit and receive polarizations, as well as measurements of the phase difference between polarizations. In this paper we refer to the linear polarizations as H and V, for horizontal and vertical respectively, and transmit/receive combinations as, e.g., HV for horizontal transmit/vertical receive. Several radar passes were obtained in the TOPSAR mode, a single-pass, dual-antenna interferometric topographic SAR [*Zebker et al.*, 1992], using the C band wavelength (Figure 2b). This mode produces an ortho-rectified C band VV polarization SAR image, elevation measurements at 5 m postings, and an interferometric phase coherence value for each pixel.

[8] The three Inyo domes analyzed are Deadman Dome, Glass Creek Dome, and Obsidian Dome (Figure 1). Polarimetric data were collected on a due south flight line, with images illuminated from the west. Incidence angles ranged from 23.9° to 53.3° for the entire set of observations of the domes; in a given image, the incidence angles across a single dome may vary as much as 11°. Data were processed in a slant range geometry, at a pixel spacing of 6.66 m in slant range and 8.10 m in azimuth. Calibration of the data was based on analysis of corner reflector signatures from the Rosamond test site obtained during the same flight season. Absolute uncertainties in calibration are 3 dB, between wavelength channels 1.5 dB, and between polarizations at a single wavelength 0.5 dB [*Lou et al.*, 1996].
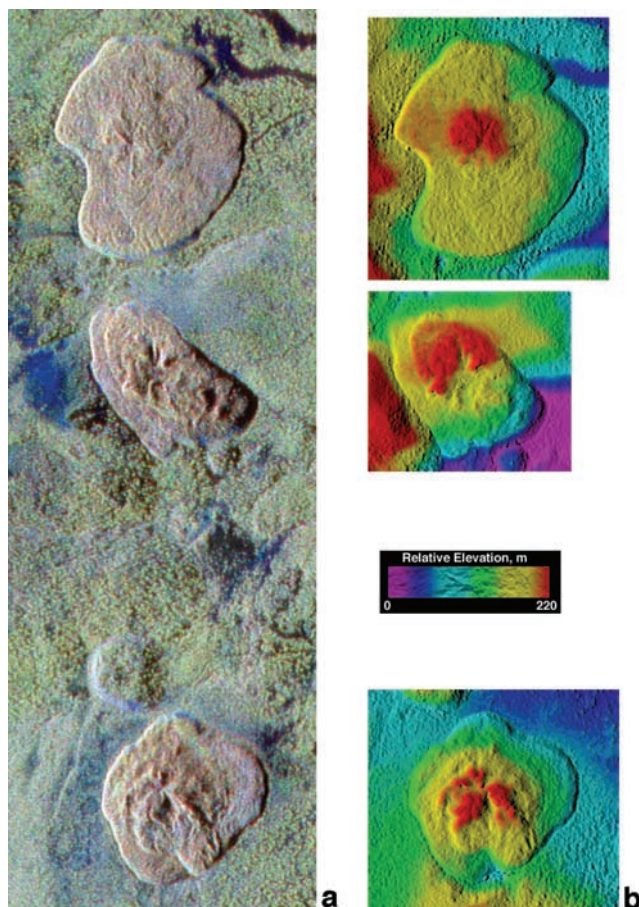
Figure 2. Radar data of Inyo domes. a) AIRSAR HV polarization color composite; blue = C band, green = L band, red = P band. Brightness proportional to σ^0 in dB, with identical contrast stretch in all bands. Reddish color on dome surfaces indicates that P band contains the highest HV σ^0 values. North is toward the top. Illumination is from the left. Incidence angles on the domes are 45°–51°. Domes, south to north: Deadman, Glass Creek, Obsidian. Swath is 7 km long. b) TOPSAR-derived digital elevation maps. Elevations are relative to an arbitrary base level for each dome. Each dome shows total relief of ∼150 m. Overall profile is convex-up for all domes, with highest topography in the central vent regions.

[9] The AIRSAR data set of the Inyo domes is diverse in incidence angle, polarization and wavelength. In this section, the variation of backscatter cross section (also known as the backscatter coefficient or sigma zero, σ^0) is examined as a function of these three parameters. Because the data are well-calibrated, comparisons of the behavior of these parameters are readily made with observations of other surface types.

3.1. Backscatter Trends

[10] Figures 3a and 3b show σ^0 values for two of the Inyo domes, Deadman and Obsidian domes, as a function of incidence angle, for the co-polarization (HH) and cross-polarization (HV) modes. Values were extracted from the entire upper surface of each dome, i.e., not including the steep margins which show strong artifacts in σ^0 values due to local incidence angle effects. Plotted values are the median σ^0, which is used to describe the "typical" scattering behavior. The median values differ from the arithmetic means by no more than 2 dB, and standard deviations from the mean are typically in the range of 2–4 dB. Each point on the plots represents several hundred pixels, each 8.10 m in azimuth by 6.66 m in slant range.

[11] The σ^0 values shown in Figure 3 imply that the dome surfaces are extremely rough, based on the high values and the negligible decrease with incidence angle. Comparison to typical basaltic lava flow surfaces at Kilauea Volcano, Hawaii (Figures 3c and 3d; see *Campbell and Campbell* [1992] for an earlier analysis of these AIRSAR data of Kilauea) indicates that the silicic dome surfaces have a distinct backscatter signature. HH σ^0 values on the domes are higher at all three wavelengths than on both a'a and pahoehoe flows on Kilauea. Moreover, the dome HH values show little dependence on wavelength, whereas the Kilauea values generally decrease as the wavelength increases. Pahoehoe flows show a systematic decrease from C to L to P band, while a'a flow values are similar at C and L, but lower at P. The silicic domes are apparently "rough" at all three wavelength scales.

[12] HV σ^0 values show an unexpected behavior, apparently unique to silicic lava flows. HV σ^0 is seen to *increase* slightly with increasing wavelength. This result is robust within the inter-channel calibration uncertainties, at least for the observation that P and L HV values exceed C band values. This trend is opposite to that observed on the Kilauea flows, where both a'a and pahoehoe flows have P band HV σ^0 values that are consistently 5–10 dB less than C band (Figures 3c and 3d).

3.2. Polarization Ratios

[13] The polarization diversity of the AIRSAR data set can be utilized to show variations of σ^0 as a function of polarization. It is useful to compare backscatter at two polarizations as a ratio, of either circular or linear polarization pairs. The circular polarization ratio, μ_c, is the ratio of the power in the circular polarization transmitted and received in the same rotation sense (SC, also known as LL for "left-left") to the power in the circular polarization transmitted in one rotation sense and received in the opposite sense (OC, also known as LR for "left-right"). A single specular reflection event is expected to reverse the circular polarization sense, giving backscattered power exclusively in the OC component. Double reflections (from "dihedral" corner reflectors), coherent backscatter effects [*Hapke*, 1990], and diffuse scattering can all contribute to the SC component, giving a $\mu_c > 0$. Circular polarization ratios in excess of unity are observed on a variety of icy surfaces, including the icy Galilean satellites [*Ostro et al.*, 1992], the polar regions of Mars [*Muhleman et al.*, 1991] and Mercury [*Slade et al.*, 1992], terrestrial ice sheets [*Rignot et al.*, 1993; *Rignot*, 1995] and glaciers [*Haldemann*, 1997]. On rocky surfaces, μ_c values are typically less than unity, with several notable exceptions. Portions of the blocky basaltic andesite SP lava flow (AZ) were reported by *Campbell et al.* [1993] to show $\mu_c > 1$ at L band. Certain regions in the
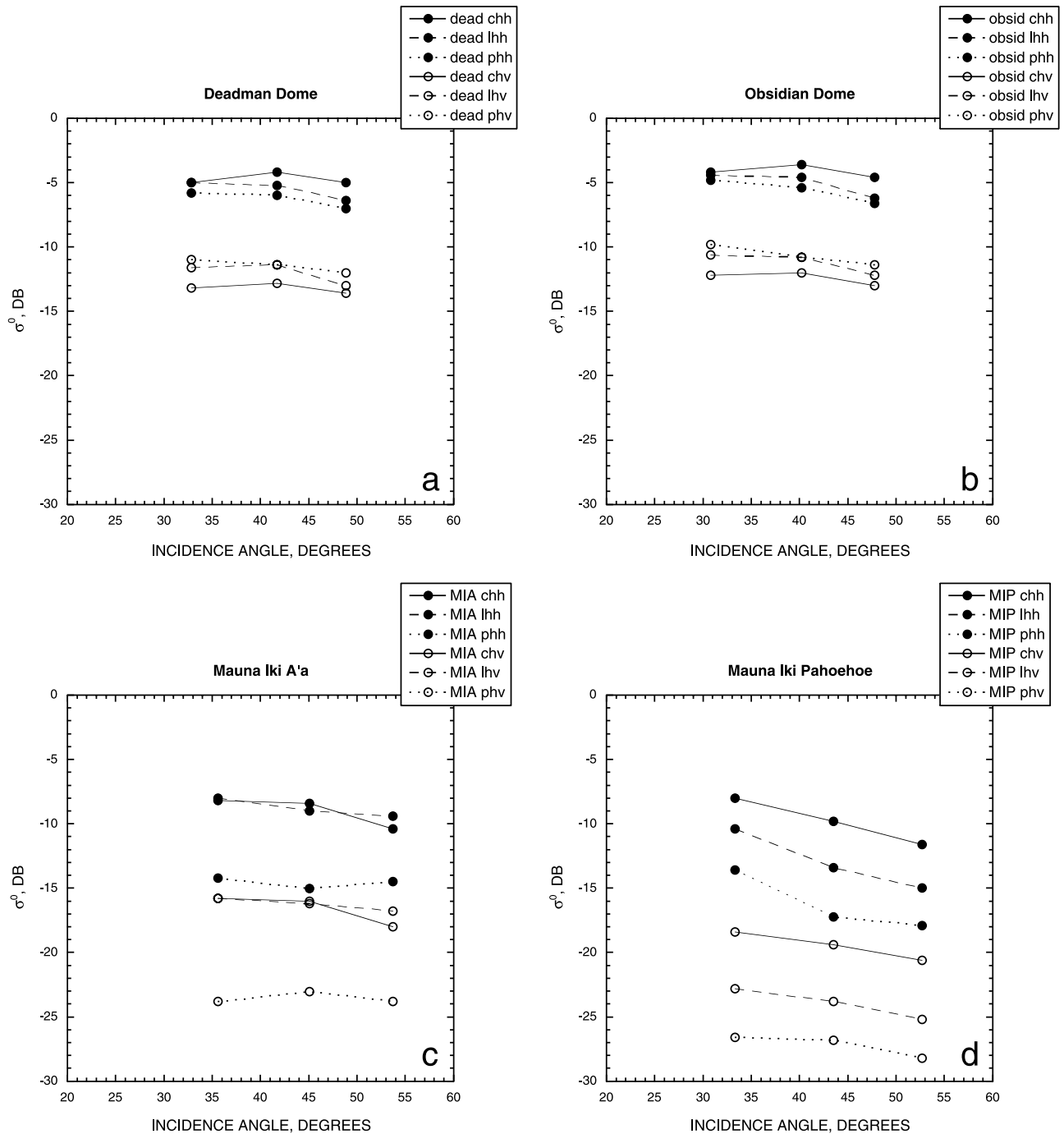
Figure 3. HH (solid symbols) and HV (open symbols) backscatter cross section, σ^0, as a function of incidence angle for two of the Inyo domes and two lava flow surfaces at Kilauea, Hawaii. Data at three wavelengths are shown: C band (5.6 cm; solid lines), L band (24 cm; dashed lines) and P band (68 cm; dotted lines). a) Deadman Dome. b) Obsidian Dome. HV values on dome surfaces show direct dependence on wavelength (P band is highest), unlike most geologic surfaces. c) A'a lava. d) Pahoehoe lava. P band values are lowest for both HH and HV, on both Kilauea lava types. Well-behaved inverse dependence on wavelength for pahoehoe surface suggests sub-wavelength roughness controls the scattering, with no "saturation" effect.

reflective highlands of Venus have also displayed $\mu_c > 1$ in Earth-based radar observations [*Tryka and Muhleman*, 1992; *Campbell et al.*, 1999].

[14] Polarization ratios of the Inyo dome surfaces and Kilauea flows are shown in Figure 4. The dome surfaces show a wide separation in μ_c values at the three AIRSAR wavelengths, with C band values of 0.3–0.4, L band 0.6–0.7 and P band 0.8–0.95. The dome μ_c values also show a slight decrease with incidence angle. Kilauea flows show lower μ_c values, and a much smaller separa-
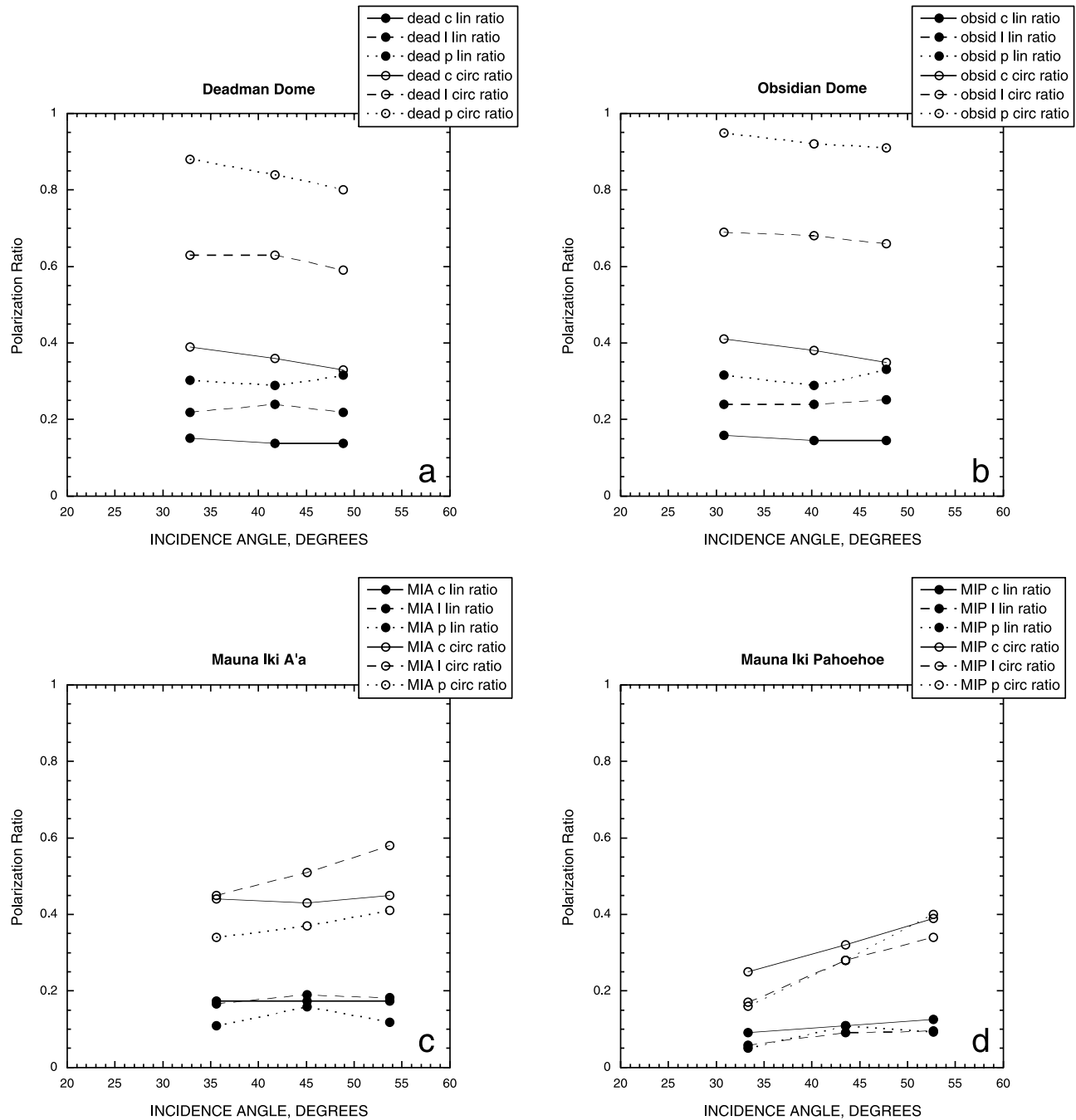
Figure 4. Linear (μ_l = HV/HH; solid symbols) and circular (μ_c = SC/OC; open symbols) polarization ratios as a function of incidence angle for two of the Inyo domes and two lava flow surfaces at Kilauea, Hawaii. Data at three wavelengths are shown: C band (solid lines), L band (dashed lines) and P band (dotted lines). a) Deadman Dome. b) Obsidian Dome. Strong wavelength dependence is seen on the domes, with highest polarization ratios at P band. P band μ_c values approach unity, indicating a possible double-bounce component. c) A'a lava. d) Pahoehoe lava. Note the lower values than those of the Inyo domes, especially P band μ_c, which does not exceed 0.5 on Kilauea flows.

tion with wavelength. Values on a'a flows are in the range 0.3–0.6, and pahoehoe flows 0.15–0.4 for all wavelengths. All Kilauea flows show an increase in μ_c with incidence angle. The most striking difference in circular polarization behavior is the strong wavelength-dependence of μ_c for the dome surfaces, with values approaching unity at P band.

[15] The linear polarization ratio, μ_l, is the ratio of the backscatter at HV polarization to that at HH. Scattering from randomly distributed dipoles is predicted to produce μ_l = 1/3 [*Long*, 1965]. Values of μ_l > 1/3 may indicate unusual scattering behavior, and have been observed on ice sheets and glaciers [*Rignot et al.*, 1993; *Rignot*, 1995; *Haldemann*, 1997] at C band, on the Galilean satellites at

Table 1. Morphometric Parameters of Inyo Domes, Derived From TOPSAR Digital Elevation Data

Dome	Diameter, km	Max. Height, m	Aspect Ratio	Volume, km³
Deadman	1.25	138	0.110	0.0669
Glass Creek	1.04	134	0.128	0.0513
Obsidian	1.53	129	0.084	0.0960

Table 2. Topographic Parameters from 83 Transects of Inyo Dome Surfaces[a]

	Min	Mean	Max
Rms height, cm (20 m)	20.4	62.0	198
Rms height, cm (1 m)	13.0	28.3	50.0
Rms slope, deg. (1 m)	12.1	27.7	43.3
Rms slope, deg. (25cm)	28.6	48.7	63.4
Fractal dimension	1.18	1.57	1.84

[a]Rms heights are given for profile segments of 20 m and 1 m. Rms slopes are given for horizontal step sizes of 1 m and 25 cm.

S band (13 cm [*Ostro et al.*, 1992]), and in the Venus highlands at S band [*Campbell et al.*, 1999]. Values of μ_l on lava flows are shown in Figure 4. A similar behavior to that observed for μ_c is seen for μ_l: μ_l shows a strong wavelength dependence, with the highest values (about 0.3) at P band. The dome μ_l values are generally higher than those of the Kilauea flows, especially at the longer wavelengths. At C band, the highest μ_l values are seen on the Kilauea a'a flows. Little incidence angle dependence is seen for any of the flow surfaces.

3.3. TOPSAR Digital Topography

[16] Figure 2b shows digital elevation data for the Inyo domes, obtained by the TOPSAR C band mode of the NASA/JPL AIRSAR radar system. These topographic data have a lateral spacing of 5 m, with a relative vertical accuracy of about $1-3$ m [*Madsen et al.*, 1995]. High resolution digital topographic data allow direct measurements of large-scale morphological characteristics of the Inyo domes. Table 1 gives the average diameter, maximum height above the average base level of the surroundings, aspect ratio and total dome volume. Volumes were estimated by summing all digital values of height with respect to the average base level of the surroundings.

[17] The TOPSAR data shown in Figure 2b clearly display the general convex shape of the Inyo domes, with the highest elevations in the central vent areas. The average slope from the vent summit to the lip above the dome margin for Deadman Dome is $10.6°$, for Obsidian Dome, $4.9°$. Glass Creek Dome apparently erupted onto terrain of significant relief, making average slope estimates more difficult to extract.

4. Field Observations

[18] In order to characterize the flow surface geometric structure responsible for the observed scattering signatures, we collected two types of field data at sites on the Inyo domes: microtopographic transects and block size frequency distributions.

[19] We selected representative sites within each of the morphologic surface types (vent, jumbled and ridged [*Anderson et al.*, 1998]), for each of the Inyo domes. Figure 5 is a field photograph of typical ridged site. Perpendicular 20 m transects were marked with a taut line. Surface heights relative to the lines were measured at a horizontal spacing of 25 cm. Data reduction included: detrending, RMS height (standard deviation of surface heights, in profile segments of 20 m and 1 m [*Shepard et al.*, 2001]), RMS slope (standard deviation of point-to-adjacent-point slopes, at spacings of 25 cm and 1 m), and fractal dimension, fit at the scale of 25 cm to several m (variogram method; see *Shepard et al.* [1995] and *Campbell and Shepard* [1996]). Table 2 summarizes the topographic parameters for the 83 transects measured. Figure 6 shows histograms of the RMS height and RMS slope measurements. As noted by *Shepard et al.* [2001], the Inyo dome surfaces represent the extreme example in surface roughness

Figure 5. Measurement site at Deadman Dome. Note ubiquitous blocks, up to several meters in size (person at left for scale).
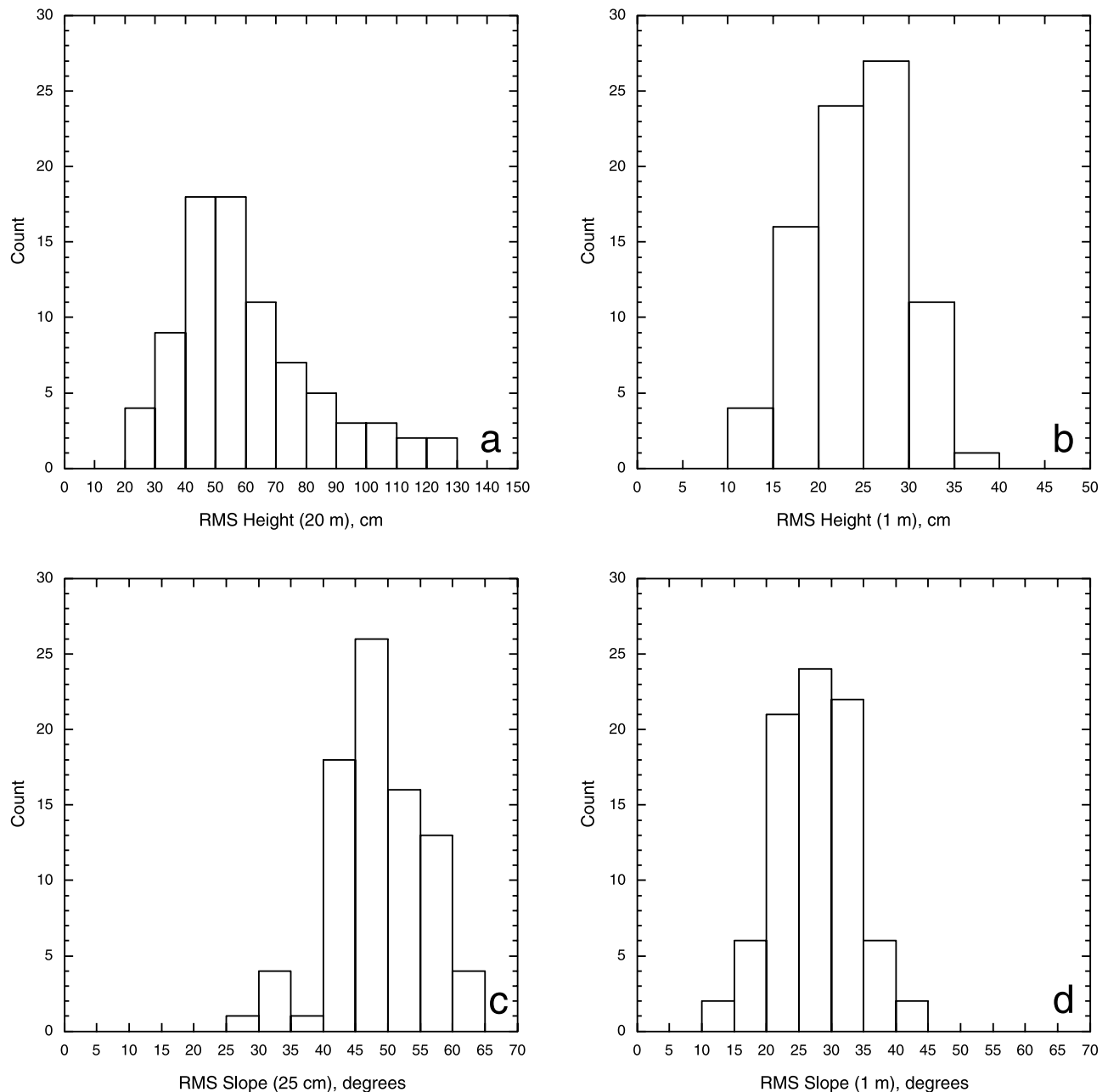
Figure 6. Histograms of topographic parameters measured along 83 detrended transects on the Inyo domes. a) RMS height at full 20 m profile length (mean = 62.0 cm), b) mean RMS height at 1 m "profile length" (mean = 28.3 cm), c) RMS slope at 25 cm horizontal step size (mean = 48.7°), d) RMS slope at 1 m horizontal step size (mean = 27.7°). The Inyo dome surfaces are among the roughest geologic surfaces ever measured [*Shepard et al.*, 2001].

compared to other natural geologic surfaces. For example, the largest value in RMS height in 1 m profile segments other than the Inyo domes is 18.7 cm, on a Kilauea a'a flow, which is well below the mean value of the dome surfaces.

[20] Block sizes were measured along each of the topographic transects. The length of each block was measured in the direction of the transect. This is analogous to the method used to determine crystal size distributions in rock thin sections; if the objects are randomly oriented, any one-dimensional measurement of size should give an average size distribution [*Cashman*, 1988; *Cashman and Marsh*,

1988]. All blocks larger than 12 cm were measured. Analysis of the block size frequency distribution data is given by *Anderson et al.* [1998]. The average block size measured on the Inyo domes was 43.3 cm. The cumulative block size frequency distributions consistently show an exponential form, especially at sizes from 12 to 50 cm. At larger block sizes, the form of the distribution sometimes departs from the exponential form observed at sizes <50 cm. For most such cases, the number of large blocks was greater than that predicted by fitting an exponential function to the population of smaller blocks [*Anderson et al.*, 1998]. Figure 7 is a
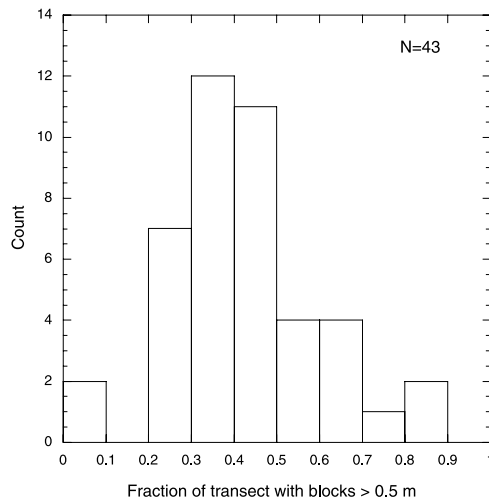
Figure 7. Histogram of the fraction of the block-count transect occupied by blocks larger than 50 cm. Values are averages from multiple transects for each of the 43 sites. A majority of the sites have more than 30% of the surface covered with blocks larger than 50 cm.

histogram of the fraction of the block-count transect occupied by blocks larger than 50 cm. At a majority of the sites, more than 38% of the surface was occupied by blocks larger than 50 cm. At 10 of the 43 sites, more than 50% of the surface was occupied by blocks larger than 50 cm.

5. Scattering Models

[21] A complete model of the radar interactions with the dome surfaces needs to account for the following characteristics observed in the scattering behavior: high backscatter cross sections at all wavelengths and polarizations, shallow scattering law slopes, weak wavelength dependence of σ^0 at HH, direct wavelength dependence at HV, strong direct dependence of circular and linear polarization ratios on wavelength, high μ_c values at P band (0.8–0.95), and weak variation of μ_c with incidence angle. Table 3 summarizes the behavior as compared to basalt flows, and as a function of wavelength and incidence angle.

[22] The domes' polarization ratios show two important trends that distinguish them from the Kilauea flows: much higher values at the longer wavelengths (P and L), and a strong direct wavelength dependence of μ_c and μ_l [$\mu P) > \mu L$) > μC)].

[23] The dome surfaces are clearly extreme in their roughness, based on field measurements and suggested by the high backscatter and shallow scattering laws. The nature of the roughness—large blocks with typically smooth faces and sharp linear edges—is quite different from that usually encountered in rough surface scattering, such as that of the Kilauea flows. This unusual morphology suggests that the radar signatures of these surfaces may result from different contributions of scattering mechanisms than those encountered on normal rough surfaces. We can rule out penetration and volume scattering as the surface materials are predominantly dense rhyolite (with only minor pumice and obsidian), and because the polarization signatures are inconsistent with those predicted for volume scattering.

[24] Several models for rough surface scattering may be applicable to the Inyo observations, and as we will show, more than one mechanism may have to be considered to fully explain the observed scattering. We evaluate the contributions of two mechanisms, one described by a rough surface (specular points or facet) scattering model and the other by an edge or dipole scattering model. The relatively large number of blocky boulders might lead one to consider the so-called incoherent component of scattering from a very rough surface. This scattering is applicable when the surface roughness is such that $kh > 5$ [*Barrick*, 1968, 1970], where, k is the radar wave number ($\frac{2\pi}{\lambda}$) and h is the surface RMS height. The measurements of RMS height at the shorter length scales (Table 2) suggest that even at P band this condition might be met. This model considers scattering that is dominated by the incoherent returns from specular points on the surface. An example of the predicted co-polarized scattering cross section of this model is [*Barrick*, 1970]

$$\sigma^0 = \frac{\sec^4 \theta}{s^2} \left| \frac{\sqrt{\varepsilon} - 1}{\sqrt{\varepsilon} + 1} \right|^2 \exp\left[-\frac{1}{s^2} \tan^2 \theta \right] \qquad (1)$$

This particular expression is valid for a surface with a Gaussian surface height probability function, where s is the surface RMS slope (for a Gaussian surface), ε is the surface dielectric constant, and θ is the radar incidence angle. Note that the quantity s is defined in a theoretical sense as twice the ratio of the surface RMS height to the surface correlation length. The interpretation of this quantity as the RMS slope of the surface is theoretically only correct for a surface with a Gaussian correlation function. The assumption of a Gaussian function is mathematically convenient, but may not be applicable to all natural surfaces. The specular points model predicts the cross-polarized return in the backscatter direction to be zero, which is clearly not the case for the dome surfaces.

[25] The specular points model, at first glance, appears to predict a radar cross section that is independent of the radar frequency. In reality, this model is derived assuming that the local radius of curvature is large compared to the radar wavelength. In practice, this means that at lower frequencies, only the larger scale scatterers will scatter according to the specular-point theory. These larger scale scatterers typically have smaller RMS slopes, as can be seen from the measurements shown in Figures 6c and 6d. The more gentle slopes at the larger spatial scales will result in lower cross sections at lower frequencies. If we assume the appropriate spatial scale to use to be several wavelengths (numerical scattering simulations suggest 2–3 wavelengths), we would need to use measurements on the order

Table 3. Summary of Scattering Behavior Observed for Inyo Dome Surfaces

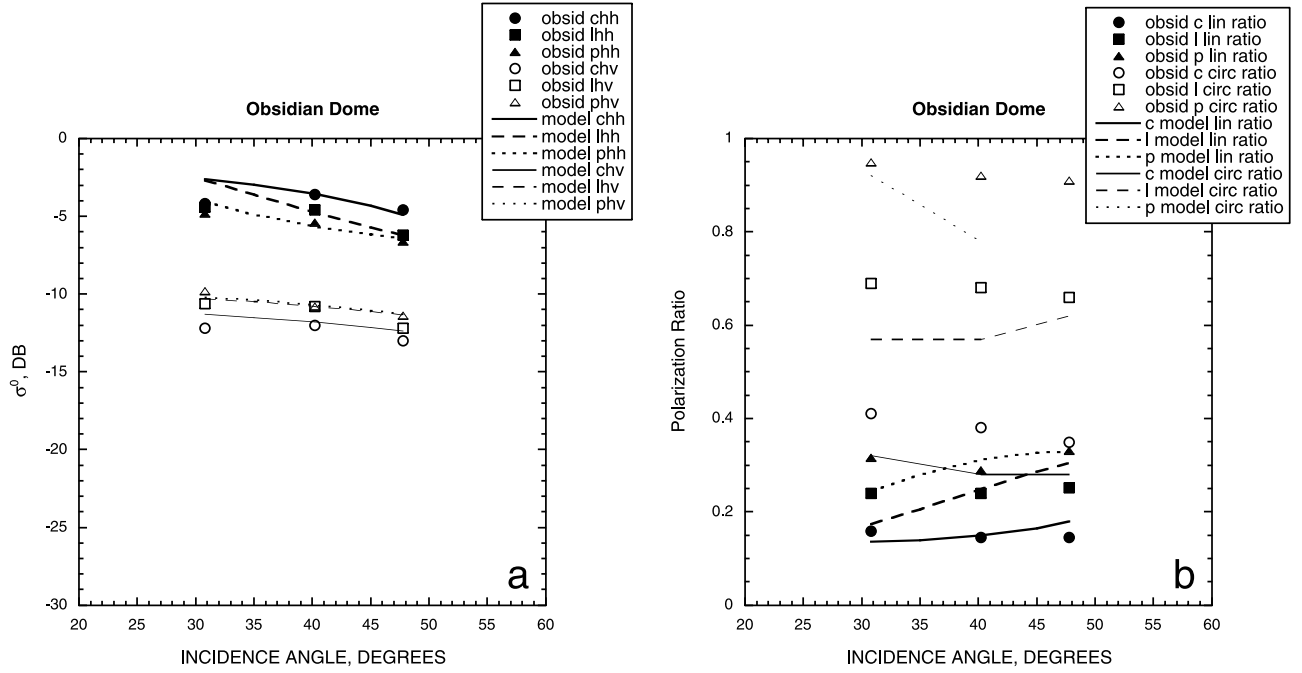| Parameter	Compared to Basalt Flows	As Wavelength Increases	As Incidence Angle Increases
σ^0 HH	high	decreases	flat
σ^0 HV	high	increases	flat
μ_c	high	increases	flat
μ_l	high	increases	decreases

Figure 8. a) Scattering model results (lines) compared with observations (symbols) for σ^0. Bold lines and symbols are HH σ^0 at the three wavelengths; thin lines and open symbols are HV σ^0. Note that the model replicates the unusual direct wavelength dependence of HV backscatter (i.e., P and L band exceed C band). b) Scattering model results (lines) compared with observations (symbols) for polarization ratios. Bold lines and symbols are linear polarization ratios, μ_l, at the three wavelengths; thin lines and open symbols are circular polarization ratios, μ_c. Circular polarization trends are well reproduced by the model, though a mismatch in magnitude suggests an unmodeled component may contribute the high μ_c (see text).

of 20 cm for C band, 75 cm for L band, and about 2 m for P band. At 2 m spacing, the average RMS slope is about 18 degrees, with a significant fraction of the slopes as high as 30 degrees. At L band, the average is in the range of $25-30$ degrees, and at C band $45-50$ degrees.

[26] On the basis of these observations one would expect to see lower co-polarized cross sections at P band than at L band and C band, consistent with observations. We used the measured RMS slope at the appropriate scale and equation (1) to calculate a weighted average of the expected radar cross section. However, such a model failed to predict the observed behavior. The predicted cross-section values are lower than observed, and the differences between the predicted cross sections at the various frequencies are much larger than observed. In addition, since the specular points model does not predict any cross-polarized return, this model by itself would not be able to completely explain the dome (or for that matter, the Kilauea) observations.

[27] *Campbell et al.* [1993] suggested that scattering from randomly oriented linear edges of surface rocks contributes a dipole component to the scattering. Randomly oriented dipoles and randomly oriented thin cylinders have been used as a model to explain the observed scattering from vegetated surfaces [*van Zyl*, 1985, 1992]. In the limit where the cylinders are thin compared to the radar wavelength (as would be the case if line sources are created by the concentration of electrical charge at the edges of rock surfaces), one would expect a linear polarization ratio as high as 1/3. Therefore it is conceivable that the edges of the

blocky surfaces such as those present on the Inyo domes make a significant contribution to the observed linear polarization ratio. We hypothesize that the total scattering is the incoherent sum of rough surface and edge scattering. We denote the ratio of the two mechanisms as R:

$$R = \frac{\mu_l}{0.33 - \mu_l}; \quad 0 \le \mu_l \le 0.33 \qquad (2)$$

The total co-polarized return would be

$$\sigma^o_{hh} = \sigma^o_{hh\,rough}(1 + R) \qquad (3)$$

where $\sigma^o_{hh\,rough}$ represents the co-polarized return from the rough surface ("specular points") scattering only. The expected angular variation in the edge scattering is similar to that observed for a layer of randomly oriented cylinders. Since there is no intrinsic difference in the scattering geometry, other than the projection of the incoming wave onto the layer, a cosine variation with angle of incidence is expected.

[28] Using the measured linear depolarization ratios, we can then calculate the required ratio of the two scattering mechanisms. The result must be self-consistent in the sense that we should then be able to use the calculated ratio to find the expected co-polarized cross section, and this prediction must be consistent with the observations.

[29] We implement the model as follows: we first predict the specular points scattering contribution, using the field
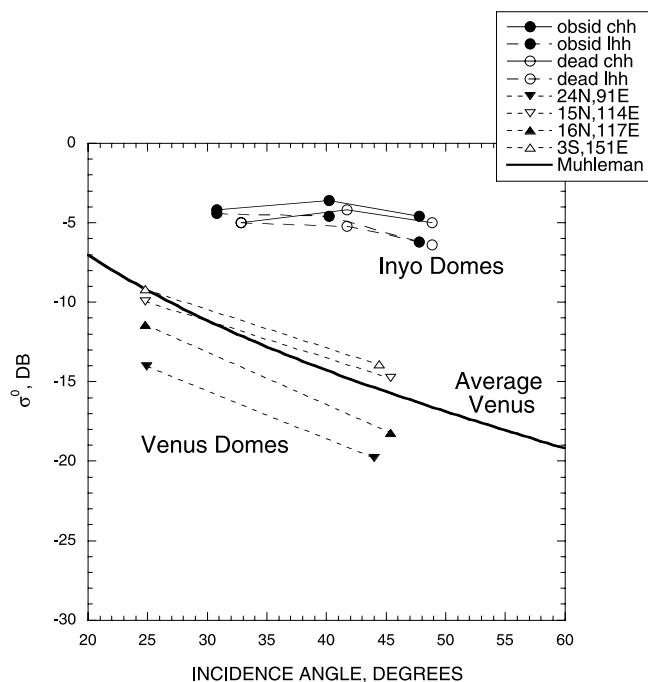
Figure 9. Comparison of backscatter measurements for terrestrial and Venusian domes. Latitude and longitude locations of the Venus domes are indicated in the legend. Magellan data for Venus are at S band wavelength (12.6 cm), which is bracketed by AIRSAR's C and L bands. Inyo domes differ from Venusian domes in both the magnitude of σ^0 and the behavior with incidence angle. Venus domes σ^0 values are similar to or lower than the average Venus surface, which resembles smooth pahoehoe in σ^0.

measurements of RMS slope at a scale appropriate to the wavelength. To estimate the strength of the edge scattering return relative to that of the specular points, we apply the average observed linear polarization ratio to expression (2). We then assign this ratio of scattering strengths to the observations at 40°, and calculate the value of the edge scattering strength. The strength of the edge scattering at other angles is then easily calculated using the cosine of the angle of incidence. The total radar cross section is then the incoherent sum of the edge returns and the specular points returns.

[30] Results and a comparison to the cross-section data for Obsidian Dome are shown in Figure 8a. The predicted cross sections show very reasonable agreement with the observations. First, the absolute cross sections are in very good agreement with the observations, and second, the cross-polarized (HV) returns show the observed direct dependence with wavelength. The predicted angular variations are similar to the observations, although the model seems to over-predict LHH, CHH and CHV at the small incidence angles. However, the differences only slightly exceed the accuracy of the absolute calibration of our data.

[31] Model results and a comparison to the polarization data for Obsidian Dome are shown in Figure 8b. The scattering matrix formulation of the model [*van Zyl and Ulaby*, 1990] allows us to predict both linear and circular polarization ratios. Because the linear polarization ratio at

40° is used as an input to the model, the modeled ratios at that angle are required to agree with the observations. The minimal (flat) angular dependence of the linear polarization ratio is not well reproduced by the model, which predicts an increase with incidence angle. The predicted circular polarization ratios match the trends of the data well, though the magnitudes are slightly higher than observed. We suggest that an unmodeled component of dihedral (double-bounce) scattering may contribute to the higher observed values of circular polarization ratio.

[32] The model results suggest that edge scattering plays a much larger role at the longer wavelengths than does the specular points scattering, based on the ratio of contributions calculated from the linear polarization ratios in expression (2). This is not unexpected, since for a given block size, the specular return would be stronger at C band than P band because of the larger size relative to the wavelength. At the same time, the block edges may be straighter compared to the P band than to the C band wavelength. A P band scale block edge also will have a broader radiation pattern than a C band scale edge, allowing more P band energy to radiate in the backscatter direction than C band for a random collection of edges. This "forgiving" aspect of the radiation pattern at long wavelengths is often observed in AIRSAR images of linear objects such as fence- and power-lines. These effects would tend to reduce the C band edge scattering strength relative to that at P band, and ultimately produce the unusually high cross-polarization cross sections at P band.

6. Comparison to Venusian Domes

[33] SAR data acquired at Venus by the Magellan space-craft revealed a class of apparently volcanic landforms referred to as "steep-sided" or "pancake" domes [*Head et al.*, 1992; *Pavri et al.*, 1992]. *Pavri et al.* [1992] identified 145 domes, with diameters ranging from 7 to 94 km, and heights ranging from 66 m to more than 4 km. *Ford* [1994] analyzed the radar scattering properties of a subset of 20 of the Venus domes. Using an assumed topographic profile derived from the spreading of a viscous Newtonian fluid [*McKenzie et al.*, 1992], *Ford* [1994] adjusted the observed σ^0 values to "corrected" values, at a local incidence angle derived from the model profile. The dome surfaces, with bright lineament pixels filtered out, for the most part showed σ^0 values within 2 dB of the average values for all of Venus, which is dominated by smooth plains surfaces [*Pettengill et al.*, 1997]. The shape assumption used by *Ford* [1994] was likely inappropriate for some of the domes analyzed, based on visual interpretation of the morphology (e.g., presence of pits, depressed central topography, collapsed margins, etc.). Magellan σ^0 values measured directly, without resorting to assumptions of dome shape, provide an appropriate comparison to the terrestrial silicic domes.

[34] Figure 9 shows σ^0 HH values for four typical Venusian domes, each viewed at two incidence angles during the Magellan mission. For comparison, AIRSAR LHH and CHH data for the Inyo domes are also plotted. The Magellan S band wavelength (12.6 cm) is bracketed by the AIRSAR L and C band wavelengths. The Magellan spatial resolution is 100−200 m, with a radiometric accu-

racy of ±2 dB [*Saunders et al.*, 1992]. The Venusian domes show σ^0 values comparable or less than the average Venus scattering law, while the Inyo domes lie 6–12 dB above the Venus average. The Venusian domes also show a substantial decrease in σ^0 with incidence angle similar to the average Venus behavior, whereas the Inyo domes' σ^0 values show little decrease with angle. The σ^0 values and scattering laws for the Venusian domes (−10 to −20 dB at incidence angles of 25°–45°) are similar to smooth Hawaiian pahoehoe and lava pond surfaces (see Figure 3d and, e.g., *Campbell and Campbell* [1992]). The Venusian dome surfaces do not display any of the extreme roughness characteristics observed in the radar data of the Inyo domes. This suggests fundamental differences in the mechanisms of emplacement of at least the upper surfaces of terrestrial silicic domes and Venusian domes. Venusian domes are apparently devoid of large (>5 cm) blocks or fractures, indicating that the lava surface was unfragmented and perhaps never covered with a stable crust until the final stages of emplacement [*Stofan et al.*, 2000]. Alternatively, the Venusian dome surfaces may have been extensively modified since emplacement, but the smoothing of blocky surfaces required to produce the observed radar signature seems unlikely.

[35] The morphology of Venusian steep-sided domes was examined by *Pavri et al.* [1992], *Fink et al.* [1993], and *Stofan et al.* [2000]. Most domes are highly circular in plan view, and typically have steep margins (subject to radar layover in some instances). Topographic profiles of domes can sometimes be inferred from backscatter variations in a single image, and *Pavri et al.* [1992] developed a classification scheme based on inferred profiles. These classes included (inverted) bowl-shaped, flat-topped, shield-like, annular (with a depressed central area), complex, tiered, and fractured. *Pavri et al.* [1992] found the majority of the 145 domes examined were in the first two categories: inverted bowl-shaped or flat-topped. However, a survey of 175 domes with diameters >19 km [*Stofan et al.*, 2000], and analyses of stereo pairs for this study, indicate that the "annular" type profile (i.e., concave-up) is at least as common as the flat-topped or inverted bowl-shaped types. Some cases were found where stereo data show portions of the central depressed areas of domes at similar elevations to the surroundings. Only two of the domes examined by *Stofan et al.* [2000] showed evidence for elevated central vent structures that characterize many terrestrial silicic domes, including the Inyo domes.

7. Discussion and Conclusions

[36] The radar backscattering characteristics of the Inyo silicic lava domes apparently reflect the unique geometric structure of the surface roughness of the flows. The extreme roughness evident in the field measurements can explain some of the behavior, such as the negligible decrease in σ^0 with incidence angle. However, the absolute magnitudes of σ^0, and in particular the unusually weak (or even "direct") wavelength dependence, imply that the unique geometry of the roughness is also controlling the scattering behavior. While the block size frequency distributions and the estimates of fractal dimension extracted from profiling are similar in form to other geologic surfaces, we suggest that the shape of the blocks themselves (angular, equant, with

smooth sides), and the relative scales of the blocks and the radar wavelengths are the key characteristics responsible for the unique radar signatures.

[37] Our modeling of the scattering mechanism incorporates a combination of rough surface scattering and scattering from block edges. The ratio of the contributions of these scattering mechanisms varies as a function of wavelength, with the longer wavelength P and L bands dominated by the edge mechanism. We suggest that radar observations at these moderately long wavelengths can be used to identify rough blocky surfaces with characteristics similar to silicic domes. For example, a dual-polarization P or L band radar system could detect the unusually high linear polarization ratios seen only on the dome surfaces (see Figure 4), and thus identify these unique volcanic textures. In terrestrial applications, such a radar could be used to identify and monitor actively growing domes to assess volcanic hazards.

[38] In summary, our analysis of multiparameter radar scattering data of silicic dome surfaces, and field measurements of surface roughness and block size, indicate that these surfaces have characteristics that make them unique among natural geologic surfaces. They are among the roughest natural surfaces ever measured. The scale and shape of the blocks that comprise the surfaces produce radar scattering characteristics unlike those of other lava flows. In particular, the minimal wavelength dependence of backscatter values, the direct wavelength dependence in cross-polarization backscatter values, and the high and wavelength-dependent values of polarization ratios distinguish silicic lava flows from any other natural geologic surface observed by radar. Comparison of backscatter properties of terrestrial and Venusian dome surfaces indicate that the Venusian surfaces do not display these unique rough and blocky textures. This suggests fundamental differences in the mechanisms of emplacement; i.e., that the Venusian domes' surfaces were unfragmented and perhaps never covered with a stable crust until the final stages of emplacement.

References

Anderson, S. W., and J. H. Fink (1990), The development and distribution of lava textures at the Mount St. Helens dome, in *Lava Flows and Domes: Emplacement Mechanisms and Hazard Implications*, *IAVCEI Proc. Volcanol.*, vol. 2, edited by J. H. Fink, pp. 25–46, Springer-Verlag, New York.

Anderson, S. W., and J. H. Fink (1992), Crease structures as indicators of emplacement rates and surface stress regimes of lava flows, *Geol. Soc. Am. Bull.*, *104*, 615–626.

Anderson, S. W., E. R. Stofan, J. J. Plaut, and D. A. Crown (1998), Block size distributions on silicic lava flow surfaces: Implications for emplacement conditions, *Geol. Soc. Am. Bull.*, *110*, 1258–1267.

Arvidson, R. E., M. K. Shepard, E. A. Guinness, S. B. Petroy, J. J. Plaut, D. L. Evans, T. G. Farr, R. Greeley, N. Lancaster, and L. R. Gaddis (1993), Characterization of lava-flow degradation in the Pisgah and Cima volcanic fields, California, using Landsat thematic mapper and AIRSAR data, *Geol. Soc. Am. Bull.*, *105*, 175–188.

Bailey, R. A., G. B. Dalrymple, and M. A. Lanphere (1976), Volcanism, structure and geochronology of Long Valley caldera, Mono County, California, *J. Geophys. Res.*, *81*, 725–744.

Bailey, R. A., R. A. Macdonald, and J. E. Thomas (1983), The Inyo-Mono craters: Products of an actively differentiating rhyolite magma chamber, eastern California, *Eos Trans. AGU*, *64*(18), 336.

Barrick, D. E. (1968), Rough surface scattering based on the specular point theory, *IEEE Trans. Antennas Propag.*, *16*, 449–454.

Barrick, D. E. (1970), Rough surfaces, in *Radar Cross Section Handbook*, vol. 2, edited by G. T. Ruck, Plenum, New York.

Bridges, N. T. (1997), Ambient effects on basalt and rhyolite lavas under Venusian, subaerial, and subaqueous conditions, *J. Geophys. Res.*, *102*, 9243–9255.

Campbell, B. A., and D. B. Campbell (1992), Analysis of volcanic surface morphology on Venus from comparison of Arecibo, Magellan and terrestrial airborne radar data, *J. Geophys. Res.*, *97*, 16,293–16,314.

Campbell, B. A., and M. K. Shepard (1996), Lava flow surface roughness and depolarized radar scattering, *J. Geophys. Res.*, *101*, 18,941–18,952.

Campbell, B. A., R. E. Arvidson, and M. K. Shepard (1993), Radar polarization properties of volcanic and playa surfaces: Applications to terrestrial remote sensing and Venus data interpretation, *J. Geophys. Res.*, *98*, 17,099–17,113.

Campbell, B. A., D. B. Campbell, and C. DeVries (1999), Surface processes in the Venus highlands: Results from analysis of Magellan and Arecibo data, *J. Geophys. Res.*, *104*, 1897–1916.

Cashman, K. V. (1988), Crystallization of Mount St. Helens dacite: A quantitative textural approach, *Bull. Volcanol.*, *50*, 194–209.

Cashman, K. V., and B. D. Marsh (1988), Crystal size distribution in rocks and the kinetics and dynamics of crystallization: II. Makaopuhi lava lake, *Contrib. Mineral. Petrol.*, *99*, 292–305.

Eichelberger, J. C., T. A. Vogel, L. W. Younker, C. D. Miller, G. H. Heiken, and K. H. Wohletz (1988), Structure and stratigraphy beneath a young phreatic vent: South Inyo Crater, Long Valley Caldera, California, *J. Geophys. Res.*, *93*, 13,208–13,220.

Fink, J. H. (1983), Structure and emplacement of a rhyolitic obsidian flow: Little Glass Mountain, Medicine Lake Highland, northern California, *Geol. Soc. Am. Bull.*, *94*, 362–380.

Fink, J. H. (1985), Geometry of silicic dikes beneath the Inyo Domes, California, *J. Geophys. Res.*, *90*, 11,127–11,133.

Fink, J. H., and C. M. Manley (1987), Origin of pumiceous and glassy textures in rhyolite domes and lava flows, in *The Emplacement of Silicic Domes and Lava Flows*, edited by J. H. Fink, *Spec. Pap. Geol. Soc. Am.*, *212*, 77–88.

Fink, J. H., N. T. Bridges, and R. E. Grimm (1993), Shapes of Venusian "pancake" domes imply episodic emplacement and silicic composition, *Geophys. Res. Lett.*, *20*, 261–264.

Ford, J. P., R. G. Blom, J. A. Crisp, C. Elachi, T. G. Farr, R. S. Saunders, E. E. Theilig, S. D. Wall, and S. B. Yewell (1989), Spaceborne radar observations: A guide for Magellan radar-image analysis, *JPL Publ. 89-41*, Jet Propul. Lab., Pasadena, Calif.

Ford, P. G. (1994), Radar scattering properties of steep-sided domes on Venus, *Icarus*, *112*, 204–218.

Gaddis, L. R., P. J. Mouginis-Mark, R. B. Singer, and V. H. Kaupp (1989), Geologic analyses of shuttle imaging radar (SIR-B) data of Kilauea Volcano, Hawaii, *Geol. Soc. Am. Bull.*, *101*, 317–332.

Gaddis, L. R., P. J. Mouginis-Mark, and J. Hayashi (1990), Lava flow surface textures: SIR-B radar image texture, field observations, and terrain measurements, *Photogramm. Eng. Remote Sens.*, *56*, 211–224.

Greeley, R., and L. Martel (1988), Radar observations of basaltic lava flows, Craters of the Moon, Idaho, *Int. J. Remote Sens.*, *9*, 1071–1085.

Haldemann, A. F. C. (1997), Interpreting radar scattering: Circular polarization perspectives from three terrestrial planets, Ph.D. thesis, 231 pp., Calif. Inst. of Technol., Pasadena.

Hapke, B. (1990), Coherent backscatter and the radar characteristics of outer planet satellites, *Icarus*, *88*, 407–417.

Head, J. W., L. S. Crumpler, J. C. Aubele, J. E. Guest, and R. S. Saunders (1992), Venus volcanism: Classification of volcanic features and structures, associations, and global distribution from Magellan data, *J. Geophys. Res.*, *97*, 13,153–13,198.

Long, M. W. (1965), On the polarization and wavelength dependence of sea echo, *IEEE Trans. Antennas Propag.*, *AP-13*, 749–754.

Lou, Y., Y. Kim, and J. J. van Zyl (1996), The NASA/JPL Airborne Synthetic Aperture Radar system, in *Summaries of the Sixth Annual JPL Airborne Science Workshop*, vol. 2, *JPL Publ. 96-4*, pp. 51–56, Jet Propul. Lab., Pasadena, Calif.

Madsen, S. N., J. M. Martin, and H. A. Zebker (1995), Analysis and evaluation of the NASA/JPL TOPSAR across-track interferometric SAR system, *IEEE Trans. Geosci. Remote Sens.*, *33*, 383–391.

Manley, C. R., and J. H. Fink (1988), Internal textures of rhyolite flows as revealed by research drilling, *Geology*, *15*, 549–552.

McKenzie, D., J. M. McKenzie, and R. S. Saunders (1992), Pancakelike domes on Venus, *J. Geophys. Res.*, *97*, 15,967–15,976.

Miller, C. D. (1985), Holocene eruptions at the Inyo Volcanic Chain, California: Implications for possible eruptions in the Long Valley caldera, *Geology*, *13*, 14–17.

Mouginis-Mark, P. J. (1995), Preliminary observations of volcanoes with the SIR-C radar, *IEEE Trans. Geosci. Remote Sens,*., *33*, 934–941.

Muhleman, D. O., B. J. Butler, A. W. Grossman, and M. A. Slade (1991), Radar images of Mars, *Science*, *253*, 1508–1513.

Ostro, S. J., et al. (1992), Europa, Ganymede and Callisto: New radar results from Arecibo and Goldstone, *J. Geophys. Res.*, *97*, 18,227–18,244.

Pavri, B., J. W. Head, K. B. Klose, and L. Wilson (1992), Steep-sided domes on Venus: Characteristics, geologic setting, and eruption conditions from Magellan data, *J. Geophys. Res.*, *97*, 13,445–13,478.

Pettengill, G. H., B. A. Campbell, D. B. Campbell, and R. A. Simpson (1997), Surface scattering and dielectric properties, in *Venus II*, edited by S. W. Bougher, pp. 527–546, Univ. of Ariz. Press, Tucson.

Reches, Z., and J. Fink (1988), The mechanism of intrusion of the Inyo Dikes, Long Valley Caldera, California, *J. Geophys. Res.*, *93*, 4321–4334.

Rignot, E. J. (1995), Backscatter model for the unusual radar properties of the Greenland ice sheet, *J. Geophys. Res.*, *100*, 9389–9400.

Rignot, E. J., S. J. Ostro, J. J. van Zyl, and K. C. Jezek (1993), Unusual echoes from the Greenland ice sheet, *Science*, *261*, 1710–1713.

Sampson, D. E. (1987), Textural heterogeneities and vent area structures in the 600-year-old lavas of the Inyo volcanic chain, eastern California, in *The Emplacement of Silicic Domes and Lava Flows*, edited by J. H. Fink, *Spec. Pap. Geol. Soc. Am.*, *212*, 89–100.

Sampson, D. E., and K. L. Cameron (1987), The geochemistry of the Inyo volcanic chain: Multiple magma systems in the Long Valley region, eastern California, *J. Geophys. Res.*, *92*, 10,403–10,421.

Saunders, R. S., et al. (1992), Magellan mission summary, *J. Geophys. Res.*, *97*, 13,067–13,090.

Shepard, M. K., R. A. Brackett, and R. E. Arvidson (1995), Self-affine (fractal) topography: Surface parameterization and radar scattering, *J. Geophys. Res.*, *100*, 11,709–11,718.

Shepard, M. K., B. A. Campbell, M. H. Bulmer, T. G. Farr, L. R. Gaddis, and J. J. Plaut (2001), The roughness of natural terrain: A planetary and remote sensing perspective, *J. Geophys. Res.*, *106*, 32,777–32,795.

Slade, M. A., B. J. Butler, and D. O. Muhleman (1992), Mercury radar imaging—Evidence for polar ice, *Science*, *258*, 635–640.

Stofan, E. R., S. W. Anderson, D. A. Crown, and J. J. Plaut (2000), Emplacement and composition of steep-sided domes on Venus, *J. Geophys. Res.*, *105*, 26,757–26,771.

Swanson, S. E., M. T. Naney, H. R. Westrich, and J. C. Eichelberger (1989), Crystallization history of Obsidian Dome, Inyo Domes, California, *Bull. Volcanol.*, *51*, 161–176.

Tryka, K. A., and D. O. Muhleman (1992), Reflection and emission properties on Venus: Alpha Regio, *J. Geophys. Res.*, *97*, 13,379–13,394.

van Zyl, J. J. (1985), On the importance of polarization in radar scattering problems, *Caltech Antenna Lab. Rep. 120*, Ph.D. thesis, 152 pp., Calif. Inst. of Technol, Pasadena.

van Zyl, J. J. (1992), Application of Cloude's target decomposition theorem to polarimetric imaging data, *Proc. SPIE Conf. Radar Polarimetry*, *1748*, 184–191.

van Zyl, J. J., and F. T. Ulaby (1990), Scattering matrix representation for simple targets, in *Radar Polarimetry for Geoscience Applications*, edited by F. T. Ulaby and C. Elachi, pp. 17–52, Artech House, Norwood, Mass.

van Zyl, J. J., H. A. Zebker, and D. N. Held (1987), Imaging radar polarization signatures: Theory and observation, *Radio Sci.*, *22*, 529–543.

Vogel, T. A., J. C. Eichelberger, L. W. Younker, B. C. Schuraytz, J. P. Horkowitz, H. W. Stockman, and H. R. Westrich (1989), Petrology and emplacement dynamics of intrusive and extrusive rhyolites of Obsidian Dome, Inyo Craters volcanic chain, eastern California, *J. Geophys. Res.*, *94*, 17,937–17,956.

Zebker, H. A., S. N. Madsen, J. Martin, K. B. Wheeler, T. Miller, Y. Lou, G. Alberti, S. Vetrella, and A. Cucci (1992), The TOPSAR interferometric radar topographic mapping instrument, *IEEE Trans. Geosci. Remote Sens.*, *30*, 933–940.

————————————

S. W. Anderson, Department of Science, Black Hills State University, USB9102, Spearfish, SD 57799, USA.

D. A. Crown, Planetary Science Institute, 1700 East Ft. Lowell Road, Tucson, AZ 85719, USA.

J. J. Plaut and J. J. van Zyl, Jet Propulsion Laboratory, California Institute of Technology, 4800 Oak Grove Drive, Pasadena, CA 91109, USA. (plaut@jpl.nasa.gov)

E. R. Stofan, Proxemy Research, P.O. Box 338, Rectortown, VA 20140, USA.